

# Spatial Scales of Cirrus Cloud Properties

Paul F. Hein and Stephen K. Cox

Colorado State University  
 Department of Atmospheric Sciences  
 Fort Collins, Colorado 80523

June 1989

## 1. Background

Through recent observational programs, such as FIRE, the structure of the cirrus cloud layer has recently been determined to be quite complex. Work of Sassen, *et al.* (1989) with lidar, aircraft and radar found a wide range of spatial scales from generating cells of about 1 km in size to mesoscale complexes of these cells on the order of 10's km, which are imbedded in the larger cirrus cloud. Smith, *et al.* (1989) with aircraft and Grund and Eloranta (1988) with lidar also found much spatial variability in the cirrus cloud parameters.

This research in studying the spatial scales of the cirrus, used data collected during the flight legs of the NCAR Sabreliner aircraft on four days during the FIRE Cirrus IFO to study the spatial scales of the cirrus, and will concentrate on the scales of the horizontal wind. The days examined are 22, 24, 28, and 31 October 1986. A variety of conditions existed on those days. On the 22nd and the 24th, a cirrostratus deck with convective cells was sampled in the vicinity of the exit region ridge of a closed low pressure system. Starr and Wylie (1988) classified the cirrus as "closed low cirrus". The cirrus of the 28th was classified as "warm front cirrus" (Starr and Wylie, 1988) because the cirrus was found ahead of the upper level short wave trough, capping the short wave ridge. The cirrus was optically thin and tenuous. The cirrus of the 31st was classified as "cold front cirrus" (Starr and Wylie, 1988) or "jet stream cirrus" (Conover, 1960) and was found on the eastern side of a short wave trough. A jet with wind speeds of about 50 m/s was measured in the cirrus top.

## 2. Data Analysis

The spatial scales of the cloud features can be described by power spectra (or spectral density graphs) and cumulative variance graphs. The cumulative variance graphs were created by first using a Fast

Fourier Transform (FFT) to create variance spectra. The variances were then summed in a cumulative fashion from the largest scalelengths (wavelengths) to the smallest. No detrending was done to the original data, and no smoothing or averaging was done to the spectral points. All the spectral points were included. This means that the values of the first five to ten spectral points of the large scalelengths should only be considered to be qualitatively correct. The cumulative variance at smaller scalelengths should be correct because a more accurate representation of the variance at the larger scalelengths should only redistribute the energy amongst the larger scalelengths. Note that each scalelength (or wavelength) contains both a "peak" and a "valley". The following graphs of cumulative variance may be interpreted as showing the percentage of variance explained by scalelengths larger than the given scalelength.

The power spectra likewise were created using an FFT and differ from the variance spectra by only a constant factor. However, the data for the power spectra were detrended and the first five spectral points were not used. The power spectra were smoothed with a six point average.

The optical properties of a cirrus cloud resulting from the downwelling shortwave and infrared radiation can be expressed by the infrared downward effective emittance ( $\epsilon^* \downarrow$ ) and the shortwave effective extinction ( $\varsigma$ ), which are defined by the following equations.

$$\epsilon^* \downarrow = \frac{H_B^{IR} \downarrow - \bar{H}_T^{IR} \downarrow}{\sigma \bar{T}^4 - \bar{H}_T^{IR} \downarrow}$$

$$\varsigma = \frac{\bar{H}_T^{SW} \downarrow - H_B^{SW} \downarrow}{\bar{H}_T^{SW} \downarrow}$$

where  $\bar{T}$  is the mean cloud temperature,  $\bar{H}_T^{SW} \downarrow$  is the mean cloud top incident shortwave irradiance, and  $\bar{H}_T^{IR} \downarrow$  is the mean cloud top downwelling infrared

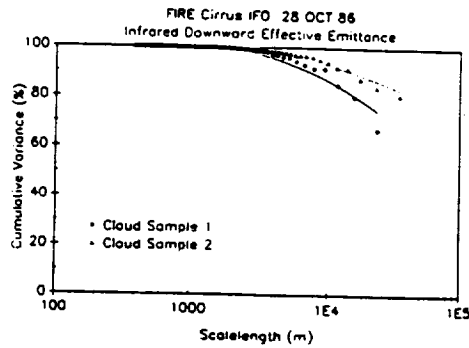


Figure 1: Cumulative variance graph of infrared downward effective emittance.

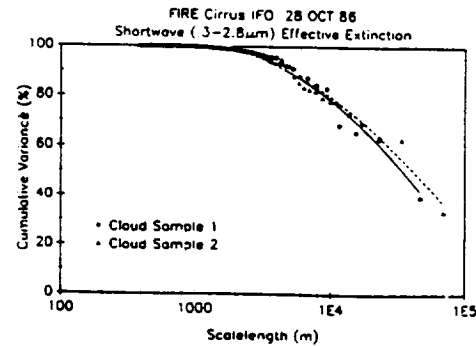


Figure 2: Cumulative variance graph of shortwave effective extinction.

irradiance. This makes  $\epsilon^* \downarrow$  and  $\zeta$  dependent only on the downwelling irradiance values ( $H_B^{SW} \downarrow, H_B^{IR} \downarrow$ ) at cloud base. Note that there may be a significant reflected component of upwelling irradiance inherent in  $\epsilon^* \downarrow$  and  $\zeta$ .

### 3. Results

The spatial scales of infrared downward effective emittance and the shortwave effective extinction are described by the cumulative variance graphs of Figures 1 and 2 for the 28th. Most of the variance is found at the large scalelengths. For the infrared downward effective emittance, 90% of the variance is explained by scalelengths larger than 10 km; and for shortwave effective extinction, 90% of the variance is explained by scalelengths larger than 5 km. Thus, most of the variability of these clouds, as seen by the Sabreliner radiometric instrumentation, is determined by the larger features. Also, the similarity between the shortwave effective extinction curves shows that the clouds have the same spatial scales even though Cloud Sample 2 is less optically thick than Cloud Sample 1. A higher percentage of the variance is found at the larger scalelengths in the infrared downward effective emittance than in the shortwave effective extinction. This is because the shortwave radiation, being highly anisotropic, is not smoothed as much by the hemispheric view of the radiometric instrumentation as is the infrared. The scales are then better represented in the shortwave effective extinction graph. The cumulative variance graphs of the 28th show this dominance of the larger scales in providing the majority of the variance, and are representative of the other days.

Representative power spectra of the alongwind and crosswind components of the horizontal wind are seen in Figures 3 to 6, and of the corresponding downwelling shortwave and infrared irradiances in Figures

7 to 10. The power spectra show a range of slopes from  $k^{-5/3}$  to  $k^{-3}$ . The wind power spectrum of the 22nd shows a  $k^{-5/3}$  slope, while the wind spectrum of the 28th shows a  $k^{-3}$  slope. The power spectra of the wind for the 24th and the 31st have a range of slopes in between the  $k^{-5/3}$  and  $k^{-3}$  slopes. The power spectra of the irradiances also have slopes constrained by the  $k^{-5/3}$  slope and the  $k^{-3}$  slope, though the slopes are not always the same as the corresponding wind spectra. It is probable that the downwelling irradiances, modulated by the cloud elements, have their scales determined by eddies of the wind.

### 4. Discussion

The slope of the power spectra of the horizontal wind can be used to determine the energy transfer between the scales. Three dimensional turbulence has a  $k^{-5/3}$  slope in the power spectra showing an energy cascade to smaller scales or larger wavenumber ( $k$ ). The power spectra of effectively two dimensional turbulence displays a  $k^{-3}$  slope and a  $k^{-5/3}$  slope in different wavenumber regions. The  $k^{-3}$  slope is a result of the transfer of eddy enstrophy (mean-squared vorticity) or the transfer of the square of quasi-geostrophic potential vorticity toward smaller scales. The  $k^{-5/3}$  slope is a result of an energy cascade to larger scales. These cascades have been described by Gifford (1988), Charney (1971) and Kraichnan (1967). Gifford (1988) suggests that in the atmosphere the net energy cascade of the two dimensional  $k^{-5/3}$  slope is to smaller scales. An alternate theory offered by VanZandt (1982) suggests the slope can be explained by internal gravity wave dynamics. However, Gage and Nastrom (1986) did not find the wave model to be completely supported by the observations. They suggested that observations of the background vertical velocity spectrum supports the wave model while the turbulence model is supported by the horizontal wind spectrum. It needs to

be noted that the two dimensional turbulence also known as geostrophic turbulence is normally applied at the synoptic scale and mesoscale motions. In this case the scales are smaller, having measured small mesoscale and large microscale motions ( $\gamma$  mesoscale and  $\alpha$  microscale as characterized by Orlanski, 1975).

The scales are likely too small for Charney's geostrophic turbulence, however, the close proximity of the tropopause and the strong temperature inversion is likely constraining the eddies with a  $k^{-3}$  slope into an effectively two dimensional flow with an enstrophy cascade. The stabilities of the layers as described in Table 1 further support this hypothesis. Table 1 contains the vertical temperature gradient for the layer, the wind shear for the layer, and the Richardson number of the layer. The Richardson number is defined as

$$Ri = \frac{g}{\theta} \frac{\partial \theta}{\partial z} \left( \frac{\partial u}{\partial z} \right)^2$$

where  $\theta$  is potential temperature,  $z$  is height,  $u$  is the wind speed, and  $g$  is the gravitational constant. The layer measured of the 22nd with the  $k^{-5/3}$  slope is the most unstable of case, while that of the 28th with the  $k^{-3}$  slope is the most stable, supporting the hypothesis that strong stability restricts the eddies to an approximate two dimensional flow.

To summarize, the majority of the variance of the cirrus cloud properties is found at the larger scales. The radiative properties of the cloud appear to have their scales determined by the surrounding eddies, which modulate the cloud elements. The amount of variance or energy contained at each scale appears to be determined by the stability of the layer, which determines whether there is a two dimensional or a three dimensional turbulent cascade.

Table 1. Stability parameters for the cirrus layer.

Day	$\frac{\partial \theta}{\partial z} \times 10^{-3}$	$ \frac{\partial u}{\partial z}  \times 10^{-3}$	Ri
22	1.9	3.3	5.1
24	2.5	3.7	5.3
28	2.9	2.1	19.2
31	3.1	4.0–4.6	4.3–5.8

## 5. Acknowledgements

This research has been supported by National Aeronautics and Space Administration under grant NAG 1-554.

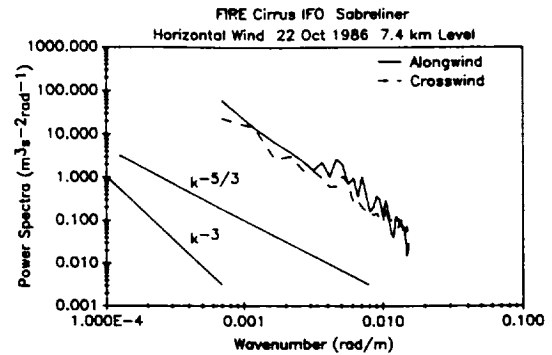


Figure 3: Power spectra of the alongwind and crosswind components of the horizontal wind: 22 Oct 1986.

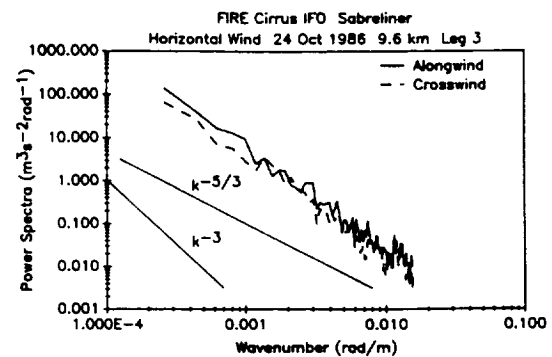


Figure 4: Power spectra of the alongwind and crosswind components of the horizontal wind: 24 Oct 1986.

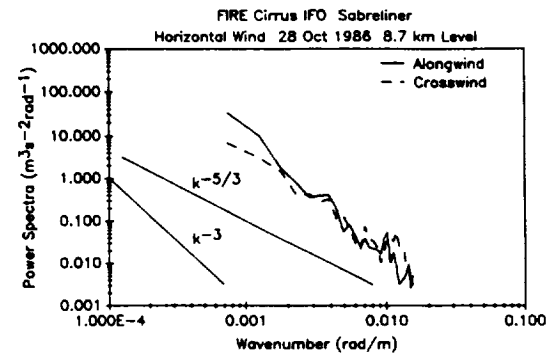


Figure 5: Power spectra of the alongwind and crosswind components of the horizontal wind: 28 Oct 1986.

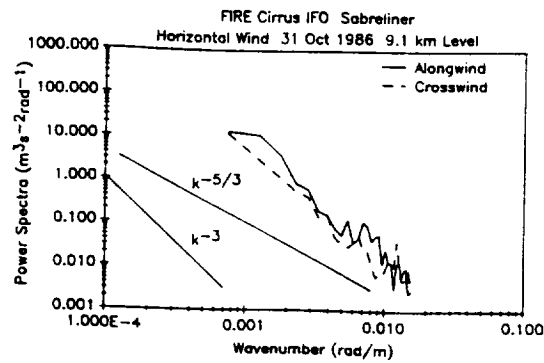


Figure 6: Power spectra of the alongwind and crosswind components of the horizontal wind: 31 Oct 1986.

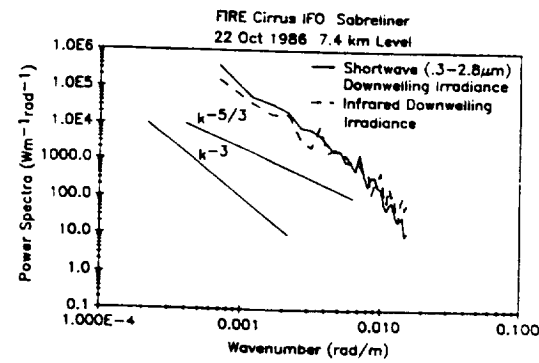
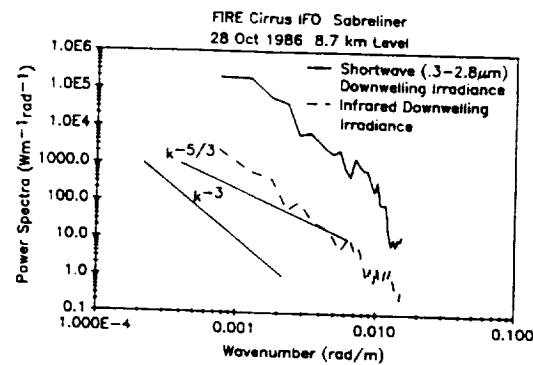


Figure 7: Power spectra of the downwelling shortwave and infrared irradiances: 22 Oct 1986.

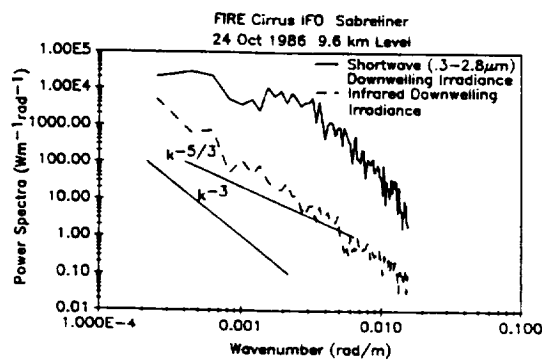


Figure 8: Power spectra of the downwelling shortwave and infrared irradiances: 24 Oct 1986.

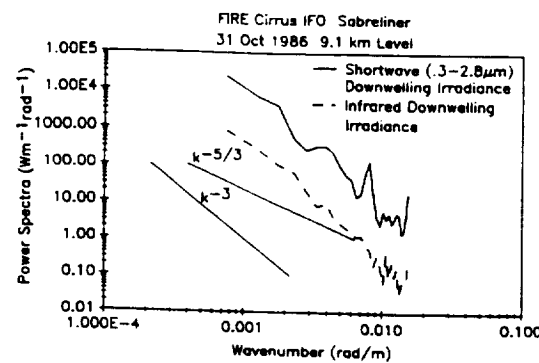


Figure 10: Power spectra of the downwelling shortwave and infrared irradiances: 31 Oct 1986.

## 6. References

- Charney, J., 1971: Geostrophic turbulence. *J. Atmos. Sci.*, **28**, 1087-1095.
- Conover, J., 1960: Cirrus patterns and related air motions near the jet stream as derived by photography. *J. Meteor.*, **17**, 532-546.
- Gage, K. S., and G. D. Nastrom, 1986: Theoretical interpretation of atmospheric wavenumber spectra of wind and temperature observed by commercial aircraft during GASP. *J. Atmos. Sci.*, **43**, 729-739.
- Gifford, F. A., 1988: A similarity theory of tropospheric turbulence energy spectrum. *J. Atmos. Sci.*, **45**, 1370-1379.
- Grund, C. J., and E. W. Eloranta, 1988: Optical and morphological properties of cirrus clouds determined by the high spectral resolution lidar during FIRE. *1988 Fire Science Team Workshop*, 52-56.
- Kraichnan, R. H., 1967: Inertial ranges in two-dimensional turbulence. *Phys. Fluids*, **10**, 1417-1423.
- Orlanski, I., 1975: A rational subdivision of scales for atmospheric processes. *Bull. Amer. Meteor. Soc.*, **56**, 527-530.
- Sassen K., D. O. Starr, and T. Uttal, 1989: Mesoscale and microscale structure of cirrus clouds: Three case studies. *J. Atmos. Sci.*, **46**, 371-396.
- Smith, W. L., Jr., P. F. Hein, and S. K. Cox, 1989: The 27-28 October 1986 FIRE IFO cirrus case study: In situ observations of radiation and dynamic properties of a cirrus cloud layer. *Mon. Wea. Rev.*, [in press].
- Starr D. O., and D. P. Wylie, 1988: Synoptic conditions producing cirrus during FIRE Cirrus IFO. *1988 Fire Science Team Workshop*, 5-12.
- VanZandt, T. E., 1982: A universal spectrum of buoyancy waves in the atmosphere. *Geophys. Res. Lett.*, **9**, 575-578.

